



**HAL**  
open science

# Early stages of $\text{UO}_{2+x}$ Sintering by in situ High-Temperature Environmental Scanning Electron Microscopy

V. Trillaud, Renaud Podor, S. Gossé, Adel Mesbah, N. Dacheux, Nicolas Clavier

► **To cite this version:**

V. Trillaud, Renaud Podor, S. Gossé, Adel Mesbah, N. Dacheux, et al.. Early stages of  $\text{UO}_{2+x}$  Sintering by in situ High-Temperature Environmental Scanning Electron Microscopy. Journal of the European Ceramic Society, 2020, 40 (15), pp.5891-5899. 10.1016/j.jeurceramsoc.2020.07.031 . hal-02927338

**HAL Id: hal-02927338**

**<https://hal.science/hal-02927338v1>**

Submitted on 1 Sep 2020

**HAL** is a multi-disciplinary open access archive for the deposit and dissemination of scientific research documents, whether they are published or not. The documents may come from teaching and research institutions in France or abroad, or from public or private research centers.

L'archive ouverte pluridisciplinaire **HAL**, est destinée au dépôt et à la diffusion de documents scientifiques de niveau recherche, publiés ou non, émanant des établissements d'enseignement et de recherche français ou étrangers, des laboratoires publics ou privés.

# **Early stages of $\text{UO}_{2+x}$ Sintering by *in situ* High-Temperature Environmental Scanning Electron Microscopy**

V. Trillaud <sup>1</sup>, R. Podor <sup>1</sup>, S. Gossé <sup>2</sup>, A. Mesbah <sup>1</sup>, N. Dacheux <sup>1</sup>, N. Clavier <sup>1,\*</sup>

1- *ICSM, Univ Montpellier, CEA, CNRS, ENSCM, Bagnols sur Cèze, France*

2- *DES, ISAS – Service de la Corrosion et du Comportement des Matériaux dans leur Environnement (SCCME), CEA, Université Paris-Saclay, F-91191, Gif-sur-Yvette, France*

**\* Corresponding author:**

Dr. Nicolas CLAVIER

Phone : + 33 4 66 33 92 08

Fax : + 33 4 66 79 76 11

[nicolas.clavier@icsm.fr](mailto:nicolas.clavier@icsm.fr)

## **Abstract**

Early stages of various uranium oxides sintering were monitored *in situ* through High Temperature Environmental Scanning Electron Microscopy. Systems composed of two  $\text{UO}_{2+x}$  microspheres were heated up to 900-1200°C under  $P_{\text{O}_2}$  ranging from  $10^{-10}$  to 25 Pa. The oxide phases stabilized were assessed through thermodynamic calculations and powder X-ray diffraction. In all the conditions tested, the formation and the development of a neck was evidenced and image processing led to quantitative data describing the morphological changes.

The evolution of the sintering degree was fitted using an exponential law and allowed the evaluation of the activation energy. When  $P_{\text{O}_2}$  led to stabilize hyper-stoichiometric  $\text{UO}_{2+x}$  oxides, the values obtained increased with  $x$ , typically in the 200-400  $\text{kJ}\cdot\text{mol}^{-1}$  range. Under air atmosphere, the stabilization of  $\text{U}_3\text{O}_8$  led to  $E_A = 260 \pm 40 \text{ kJ}\cdot\text{mol}^{-1}$ . Finally, the main diffusion mechanism driving neck formation was found to be volume diffusion, independently from the oxide stoichiometry.

## **Keywords**

Sintering – *In situ* ESEM – Uranium oxide – Calphad

## 1. Introduction

Uranium dioxide ( $\text{UO}_2$ ) and derived mixed oxides such as  $(\text{U,Pu})\text{O}_2$  are the most widely used nuclear fuels in the world, and are still considered in several concepts of Generation IV projects, including Sodium-cooled Fast Reactor (SFR) [1]. As ceramic materials, sintering constitutes a key-step of their fabrication process, in which operating conditions (i.e. temperature, heating time, atmosphere) must be carefully controlled in order to master the final characteristics of the fuel pellets, including microstructure and oxide stoichiometry. In this frame, numerous studies addressed the sintering of  $\text{UO}_{2+x}$  samples [2-5] but mainly focused on intermediate and final stages, which are characterized by grain growth and pores elimination. Conversely, the first stage of sintering, associated with the formation of necks between the grains, is generally investigated through numerical simulations, using either molecular dynamics [6], Monte Carlo [7] or Discrete Elements methods [8]. Within all of these methods, approximations are made both on the morphology of grains (supposed to be perfect spheres) and on their crystalline state (single crystal). Then, the results obtained can be hardly used to provide a predictive and reliable description of the first stage of the sintering process, which is required to optimize the elaboration of nuclear fuels. In parallel, only few experimental works were dedicated to the first stage of  $\text{UO}_{2+x}$  sintering [9-11]. Moreover, the range of temperature used in these studies, notably during dilatometry experiments, might have led the authors to encompass several phenomena, such as neck formation and densification/grain growth. Also, the exact stoichiometry of the samples frequently lacked of an accurate characterization.

This last point is particularly sensitive for uranium oxides. Indeed, uranium can adopt multiple oxidation states (mainly +IV, +V and +VI) that strongly modify the diffusion coefficients and then the sintering kinetics. As such, slightly hyper-stoichiometric oxides  $\text{UO}_{2+x}$  (with typically  $x < 0.1$ ) are generally reported to sinter at lower temperature than stoichiometric  $\text{UO}_{2.00}$  samples [3, 12-14]. Conversely, higher values of the O/U ratio, which can result in the formation of  $\text{UO}_{2+x}$  -  $\text{U}_4\text{O}_9$  mixtures, are generally associated to an increase in the activation energy attached to the sintering process [3]. Nevertheless, the modification of the kinetics with the atmosphere used, hence with the O/U ratio in the sample, received different explanations in the literature, based either on the variation of the diffusion coefficient of uranium or on different diffusion mechanisms.

In order to address these different issues, this study reports for the first time *in situ* High-Temperature Environmental Scanning Electron Microscopy (HT-ESEM) observations of the first stage of sintering of uranium oxide microspheres. These samples were selected as model compounds for real  $\text{UO}_{2+x}$  powders used in the fabrication of nuclear fuel as well as for the systems generally used in numerical simulations, composed of two spheres in contact. This approach, which allows the determination of quantitative geometrical data describing the formation then the growth of a neck between spherical particles was already developed and tested on model compounds free from redox reactions [15, 16]. In the case of the present study, this methodology has been adapted to various atmospheres in order to stabilize different uranium oxide phases. The accurate characterization of their stoichiometry in terms of O/U ratio and the associated morphological modifications observed during heat treatments at high temperature (typically in the 900-1200°C range) will be reported herein. Then, the collected data will be used to evaluate the activation energy associated to the first step of the sintering, and to point out the driving diffusion mechanism.

## 2. Experimental

### 2.1. Synthesis of $\text{UO}_{2+x}$ microspheres and sample preparation

All the chemicals used were of analytical-grade and supplied by Sigma-Aldrich, except uranium metal chips that were kindly provided by CETAMA. The synthesis of  $\text{UO}_{2+x}$  microspheres was undertaken by hydrothermal conversion of uranium(IV) aspartate following the protocol reported in [17]. The initial precursor was first obtained by mixing 0.5 mmol of U(IV) in hydrochloric media [18] with 10 mL of solution containing 1.5 mmol of aspartic acid ( $\text{C}_4\text{H}_7\text{NO}_4$ ). The hydrochloric uranium(IV) solution was added dropwise while continuously adjusting the pH to 2 with diluted ammonia, resulting in the formation of a greenish precipitate. This solid phase, together with the supernatant, was transferred into a Teflon-lined Parr autoclave, and heated at  $160^\circ\text{C}$  for 30 hours. During the hydrothermal treatment, the reactor was magnetically stirred in order to reach a Reynolds number of about  $\text{Re}_a = 13000$ . This led to set the average size of the particles to about 700-800 nm in diameter, which was found to be the optimal size to observe the sintering by HT-ESEM in a reasonable amount of time (i.e. from couple of minutes to several hours). At the end of the hydrothermal treatment, the autoclave was cooled down overnight before collecting the final precipitate. This latter was separated by centrifugation, washed twice with deionized water and twice with ethanol, and finally dried overnight at  $60^\circ\text{C}$  in an oven.

The resulting  $\text{UO}_{2+x}$  microspheres were further dispersed in 1 mL of ethanol and sonicated at 37 kHz for a few minutes. A drop of this suspension was then deposited onto the surface of a 96% pure alumina substrate (Goodfellow, 0.15 mm thickness) and let to evaporate at room temperature. This operation was reiterated 2 to 5 times in order to obtain an homogeneous deposit and to ensure the presence of sufficient amount of microspheres. With the aim to avoid any unwanted reactions with impurities coming from the substrate, alumina plates were first fired at  $1300^\circ\text{C}$  for 2 hours under air atmosphere, then washed overnight in aqua regia, and finally polished to mirror-grade. After application of this protocol, preliminary ESEM observations of the deposits revealed a very good dispersion of the  $\text{UO}_{2+x}$  microspheres at the surface of the substrate. Also, it allowed the spontaneous formation of different systems, constituted by the aggregation of 2, 3 or more microspheres (**Figure 1**).

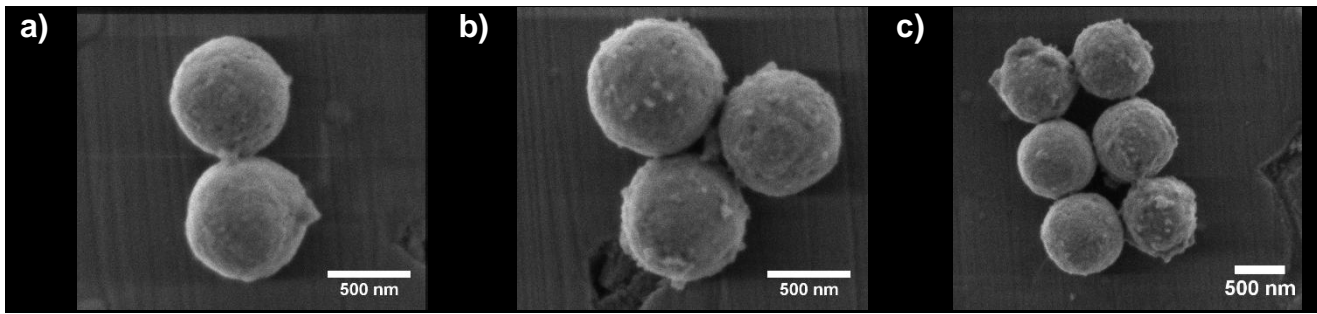


**Figure 1.** Examples of the various geometrical configurations obtained after deposition of  $\text{UO}_{2+x}$  microspheres suspension onto the surface of the alumina substrate: a) 2-grain model system, b) 3-grain system and c) complex system made of 6 microspheres.

## 2.2. Powder X-Ray Diffraction

Powder X-Ray Diffraction (PXRD) data were collected with a Bruker D8 diffractometer equipped with a Lynxeye detector in the reflection geometry with Göbel mirror and using  $\text{Cu K}\alpha_{1,2}$  radiation ( $\lambda_{\text{average}} = 1.54184 \text{ \AA}$ ). PXRD patterns were recorded at room temperature in the  $5 - 100^\circ$  range ( $2\theta$ ), a step size of  $\Delta(2\theta) = 0.01^\circ$  and a total counting time of about 3 hours per sample. All the PXRD patterns were refined by the Rietveld method using the Cox-Hastings pseudo-Voigt profile function [19] implemented in the Fullprof\_suite program [20]. Pure silicon was collected as a standard and used to extract the instrumental function.

## 2.3. HT-ESEM

HT-ESEM observation of  $\text{UO}_{2+x}$  microspheres during the first step of their sintering was operated using a Quanta 200 FEG microscope supplied by FEI – Thermo Fischer, equipped with a Gaseous Secondary Electron Detector (GSED). In order to perform *in situ* observations during heat treatments, two furnaces were used. For most of the experiments, the microscope was implemented with a  $1400^\circ\text{C}$  FEI hot stage [21], while accurate measurement of the sample temperature was performed using a homemade thermocouple integrated in the sample holder [22]. The thermocouple was calibrated by measuring the melting temperature of a gold wire, and usually provided a  $\pm 5^\circ\text{C}$  precision on measurements. For some of the experiments performed under low  $\text{P}_{\text{O}_2}$  values, a FurnaSEM hot stage (Newtec Scientific) [23] was used. In this case, duplicate experiments were run to confirm that the furnace change did not impacted our results.

In order to control the partial pressure of oxygen ( $P_{O_2}$ ) in the atmosphere surrounding the sample, then to evaluate its impact on the sintering kinetics, the experimental procedures developed by Nkou Bouala *et al.* during the study of  $ThO_2$  and  $CeO_2$  microspheres [15, 16] were slightly adapted. Different gas mixtures were employed:

- $N_2 / 5\% H_2$  mixture was initially supplied by Air Liquide. Prior its injection in the ESEM chamber, it was bubbled in a  $17^\circ C$  thermostatic water bath. This setup allowed us to control the water vapor saturation pressure, then to monitor the  $P_{O_2}$  value through the  $H_2/H_2O$  couple.

- $N_2 / 10^3$  ppm  $O_2$  supplied by Air Liquide
- ambient air

For all the gases used, the total pressure in the chamber was typically set between 100 and 150 Pa, which resulted in partial dioxygen pressures ranging from  $10^{-10}$  to 25 Pa (**Table 1**).

**Table 1.** Summary of the gas mixtures and pressures used in the ESEM chamber for the study of the first step of uranium oxides sintering.

Gas mixture	Pressure (Pa)	$P_{O_2}$ (Pa)
$N_2 / 5\% H_2 / 2.10^4$ ppm $H_2O$	150	$\sim 10^{-10}$
$N_2 / 10^3$ ppm $O_2$	100	$\sim 10^{-2}$
Air	120	$\sim 25$

Once transferred inside the microscope chamber, the samples were first heated up to  $350-400^\circ C$ . At this temperature, a short dwell allowed to get rid of the residual volatile species remaining in the particles (i.e. typically water and organics, leading to the departure of  $H_2O$ ,  $CO$  and  $CO_2$  from the sample) and to position the thermic shield above the heating stage. Heating up to the final temperature of the experiment, which ranged typically from  $800$  to  $1100^\circ C$ , was then performed under vacuum considering a high heating rate of  $50^\circ C.min^{-1}$  in order to avoid any oxidation and morphological modification of the samples before reaching the isotherm dwell. The working atmosphere was finally reinjected in the SEM chamber once the targeted temperature was reached.

High resolution images were acquired at a typical frequency of 1-60 frame per minute, which mainly depended on the scanning rate considered. Also, a significant loss of resolution was generally observed above  $1100^\circ C$ , due to the progressive increase of the thermal electrons emission with temperature [21, 24]. As high magnification images (i.e.  $60\ 000\times - 120\ 000\times$ ) were required for our study, the working temperature was then limited to around  $1200^\circ C$ .

## **2.4. Image processing**

Images of the two-grain systems recorded during isotherm thermal treatments were processed in order to achieve direct determination of quantitative data. The protocol employed followed image processing reported in our previous publications [15, 16]. Trainable Weka Segmentation plugin [25] available in the Fiji software [26] first led to the automatic extraction of grain contours. The images obtained after segmentation were then used with the custom software ImageJu [27] for the determination of the different parameters generally used in numerical models to describe the morphological modifications occurring during the first stage of sintering, such as neck size, grains size and distance between the grain centers.

## **2.5. Uncertainties determination**

The uncertainties associated to the values determined mainly depended on the scanning rate used and on the heat treatment duration. A typical relative deviation was then estimated by repeating at least 4 times neck and grains size measurement for each scanning rate considered in our experiments. During the onset of the isotherm, the images were generally blurred and/or noisy because of external perturbations due to temperature stabilization. Images were then recorded with a dwell time of 1-2  $\mu$ s per pixel (considering a typical image size of  $1024 \times 880$  pixels) and the relative error on the data was evaluated between 15% and 20%. This error further decreased gradually during the experiment with the stabilization of the image (along with that of the heating cell temperature), and reached about 5 % for dwell times comprised between 5 and 10  $\mu$ s per pixel [15].

Additionally, for all the operating conditions tested in terms of temperature and  $P_{O_2}$ , at least 3 to 4 two-grain systems were monitored all along the isothermal heat treatment. In each case, the sintering degree (defined as the ration between neck and grain diameter) was determined and was found to overlap between the different datasets, considering the error bar mentioned above.

### 3. Results and discussion

#### 3.1. Determination of oxides stoichiometry

In order to evidence the effect of the atmosphere on the first step of uranium oxides sintering, the stoichiometry of the stabilized samples was first determined by a combined approach involving thermodynamic calculations and experimental PXRD measurements. Using the Calphad (Calculation of Phase Diagram) method [28], the stoichiometry of the fluorite structure of  $\text{UO}_{2\pm x}$  was estimated from the U-O assessment after Guéneau *et al.* [29]. The O/U calculations were performed as a function of temperature for an oxygen pressure ( $P_{\text{O}_2}$ ) equal to  $10^{-10}$  Pa,  $10^{-1}$  Pa and 25 Pa under a total pressure of 101.325 kPa. The range of temperature considered was chosen owing to the technological limitations imposed by the use of HT-ESEM and by the kinetics of neck formation. As such, it was chosen so that the equilibrium was reached in several tens of minutes to several hours.

The results presented in **Figure 2** confirm the influence of the atmosphere on the evolution of the stoichiometry of  $\text{UO}_{2\pm x}$  and the possible formation of secondary oxides such as  $\text{U}_4\text{O}_9$  and  $\text{U}_3\text{O}_8$ . For the lowest dioxygen partial pressure investigated ( $10^{-10}$  Pa) (**Figure 2a**), the calculated phase diagram evidenced the formation of a slightly hyper-stoichiometric composition that could be estimated to  $\text{UO}_{2.01}$ . When the  $P_{\text{O}_2}$  value raised to  $10^{-1}$  Pa, the hyper-stoichiometry increased to about  $\text{O/U} = 2.2$  at  $1000^\circ\text{C}$ , but remained in the single phase domain of the fluorite-type structure of  $\text{UO}_{2+x}$ , which was usually reported to be stable up to  $x = 0.25$  [29-31] and calculated to be around  $x = 0.24$  (see **Figure S1** supplied as supporting information).

Finally, when the as-synthesized microspheres were heated in air atmosphere (i.e. with  $P_{\text{O}_2} = 25$  Pa), their transformation into the oxidized phase  $\text{U}_3\text{O}_8$ , which consists of a mixture of U(V) and U(VI) [32] was observed.

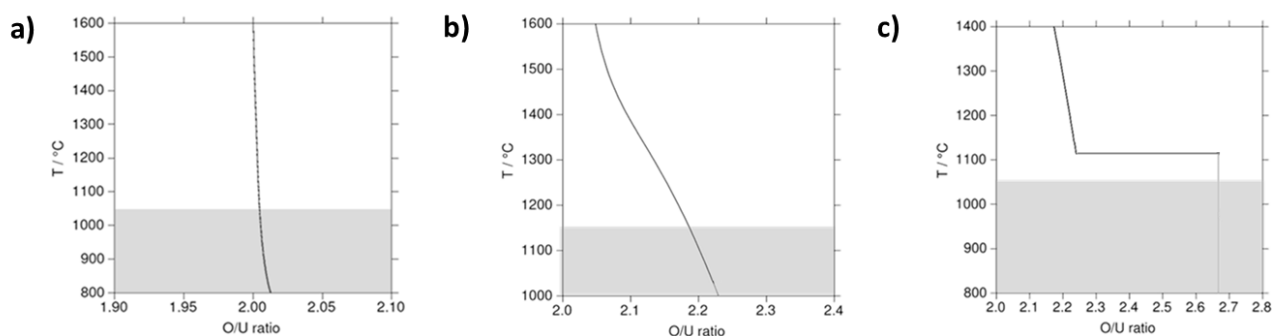


**Figure 2.** O/U equilibrium ratio calculated from Guéneau et al. [29] as a function of temperature for different oxidizing atmospheres: a)  $P_{O_2} = 10^{-10}$  Pa, b)  $P_{O_2} = 10^{-1}$  Pa and c)  $P_{O_2} = 25$  Pa. The shaded area corresponds to the temperature range investigated experimentally in this work.

The Calphad calculations were further checked by Powder X-Ray Diffraction (PXRD) measurements performed on calcined samples. With this aim, typical mass of 10 mg of as-synthesized uranium oxide microspheres were placed in a platinum crucible and fired during 1 hour at the target temperature in the heating stage of the ESEM. The operating conditions were then strictly identical to those used during the observation of the sintering processes. After cooling down to room temperature, powdered samples were placed in an inert glovebox to avoid any uranium oxidation at ambient atmosphere, then quickly analyzed by PXRD (**Figure 3**).

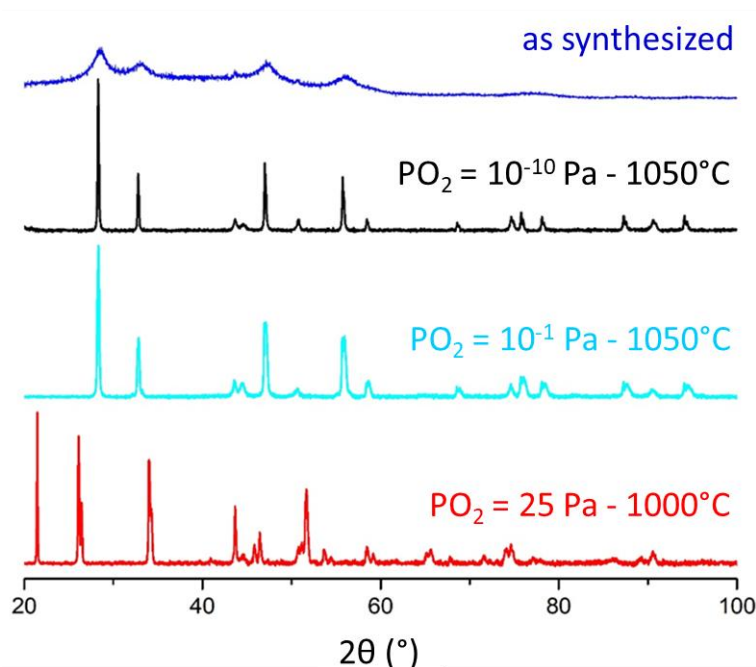


**Figure 3.** PXRD patterns recorded for the as-synthesized particles (dark blue) and for samples heated for 1 hour in various experimental conditions :  $P_{O_2} = 10^{-10}$  Pa – T = 1050°C (black) ;  $P_{O_2} = 10^{-1}$  Pa – T = 1050°C (light blue) ;  $P_{O_2} = 25$  Pa – T = 1000°C (red).

The pattern recorded for the raw microspheres exhibited the characteristic diffraction lines of the fluorite-type structure of  $\text{UO}_{2+x}$ . Nevertheless, they appear to be very wide as a consequence of the nano-structuration of the particles. Indeed, Rietveld refinement of the data showed that the average crystallite size reached around 4 nm. Conversely, all the PXRD patterns collected for calcined samples presented narrow PXRD lines. Associated crystallite sizes equaled 80 to 90 nm range depending on the conditions considered (**Table 2**). This indicated that the crystallite growth and/or the mechanical rearrangement phenomena competed with the elaboration of a neck upon heat treatment during the first step of sintering, as already evidenced for other systems such as  $\text{CeO}_2$  and  $\text{ThO}_2$  [15, 16].

For  $P_{\text{O}_2} = 10^{-10}$  and  $10^{-1}$  Pa, the PXRD diagrams obtained still matched with the fluorite-type structure of  $\text{UO}_{2+x}$ . Nevertheless, Rietveld refinement showed that the unit cell parameters were significantly modified with the variation of the dioxygen partial pressure (**Table 2**). At  $P_{\text{O}_2} = 10^{-10}$  Pa, the value determined was close to the dataset recently published by Leinders *et al.* for stoichiometric  $\text{UO}_{2.00}$  [33], which appeared in good agreement with the thermodynamic calculations. For  $P_{\text{O}_2} = 10^{-1}$  Pa, the sample analyzed at room temperature was found to be composed of two fluorite-type structures with different unit cell parameters, indicating an increase in the global O/U ratio of the sample. Indeed, the fluorite structure of uranium dioxide only accepts limited hyper-stoichiometry at room temperature, typically up to  $x = 0.05$ , and then quickly yields complex mixtures of  $\text{UO}_{2+x}$ ,  $\text{U}_4\text{O}_9$  and even  $\text{U}_3\text{O}_{8-x}$  [34]. The stoichiometry of the high-temperature phase was then estimated based on the smaller unit cell parameter ( $a = 5.4447(1) \text{ \AA}$ ), which corresponds to the higher O/U value. Indeed, the unit cell parameter was found to range between the values reported by Grønvold for  $\text{UO}_{2.20}$  ( $a = 5.4462 \text{ \AA}$ ) and for  $\text{UO}_{2.25}$  ( $a = 5.4411 \text{ \AA}$ ) [35]. A simple interpolation led to estimate the O/U ratio in our sample to 2.21, which was once again in very good agreement with the thermodynamic calculations. Finally, heating the raw microspheres under air led to a deep modification of the PXRD pattern which evidenced the oxidation of the sample towards  $\text{U}_3\text{O}_8$ . The different atmospheres employed in this study then allowed us to stabilize various uranium oxides at high temperature, allowing the investigation of *in situ* effects of the O/U stoichiometry on the first step of sintering kinetics.

**Table 2.** Unit cell parameters and average crystallite sizes of uranium oxide determined through Rietveld refinement of the PXRD data for several dioxygen partial pressures.

Reference	Sample	a (Å)	b (Å)	c (Å)	v (Å <sup>3</sup> )	Average crystallite size (nm)
[33]	UO <sub>2.00</sub>	5.4713(1)			163.781(1)	
This study	P <sub>O<sub>2</sub></sub> = 10 <sup>-10</sup> Pa	5.4704(1)			163.7(1)	90 ± 10
This study	P <sub>O<sub>2</sub></sub> = 10 <sup>-1</sup> Pa	5.4447(1)			161.4(1)	90 ± 5
		5.4680(1)			163.5(1)	
This study	P <sub>O<sub>2</sub></sub> = 25 Pa	4.1443(2)	11.8763(4)	6.7443(2)	331.95(2)	80 ± 20
[36]	U <sub>3</sub> O <sub>8</sub>	4.147(5)	11.960(2)	6.716(1)	333.09(3)	

### 3.2. General evolution of the samples morphology

Series of HT-ESEM images recorded *in situ* at 1000°C under the different atmospheres investigated are gathered in **Figure 4**, and provide an example of the general evolution of the samples morphology during the heat treatment.

For the lowest dioxygen partial pressure considered (i.e. P<sub>O<sub>2</sub></sub> = 10<sup>-10</sup> Pa), which led to stabilize the nearly-stoichiometric UO<sub>2.01</sub>, the formation and the continuous growth of a neck between the two spherical grains was clearly observed. It was accompanied by the increase of the size of the crystallites composing the particles, which was particularly obvious when comparing the micrographs collected after 6 and 18 minutes of heat treatment. Similar features were reported when working with P<sub>O<sub>2</sub></sub> = 10<sup>-1</sup> Pa, however with different kinetics. Indeed, the size of the neck increased very quickly then reached a steady-state after only 15 minutes of heat treatment at 1000°C. Simultaneously, the average crystallite size also increased up to 100 nm, which appeared in good agreement with the data obtained from PXRD analysis.

Beyond their inner microstructure, the particles were found to undergo important morphological modifications when working under air (P<sub>O<sub>2</sub></sub> = 25 Pa). During the heat treatment, the general shape evolved from spherical to ovoid, which was probably linked to the transformation of UO<sub>2+x</sub> into U<sub>3</sub>O<sub>8</sub>. Indeed, this oxidation reaction is accompanied by a 37% increase of the unit cell volumes when turning from U<sub>3</sub>O<sub>8-x</sub> (with x = 1) [37] to U<sub>3</sub>O<sub>8</sub>.

While the associated constraints can generate abundant cracking in the nuclear fuel pellets [38], there are more likely to be accommodated through deformation in the case of our sub-micrometric particles. This deformation then occurred simultaneously to the growth of the crystallites, almost immediately after injecting the gas in the HT-ESEM chamber. From the image series reported in **Figure 4**, crystallites also seemed to reach their maximum size only few seconds after the onset of the isothermal dwell. Similarly, the growth of the neck between the particles was accelerated and reached a steady-state after only 7 minutes of heat treatment.

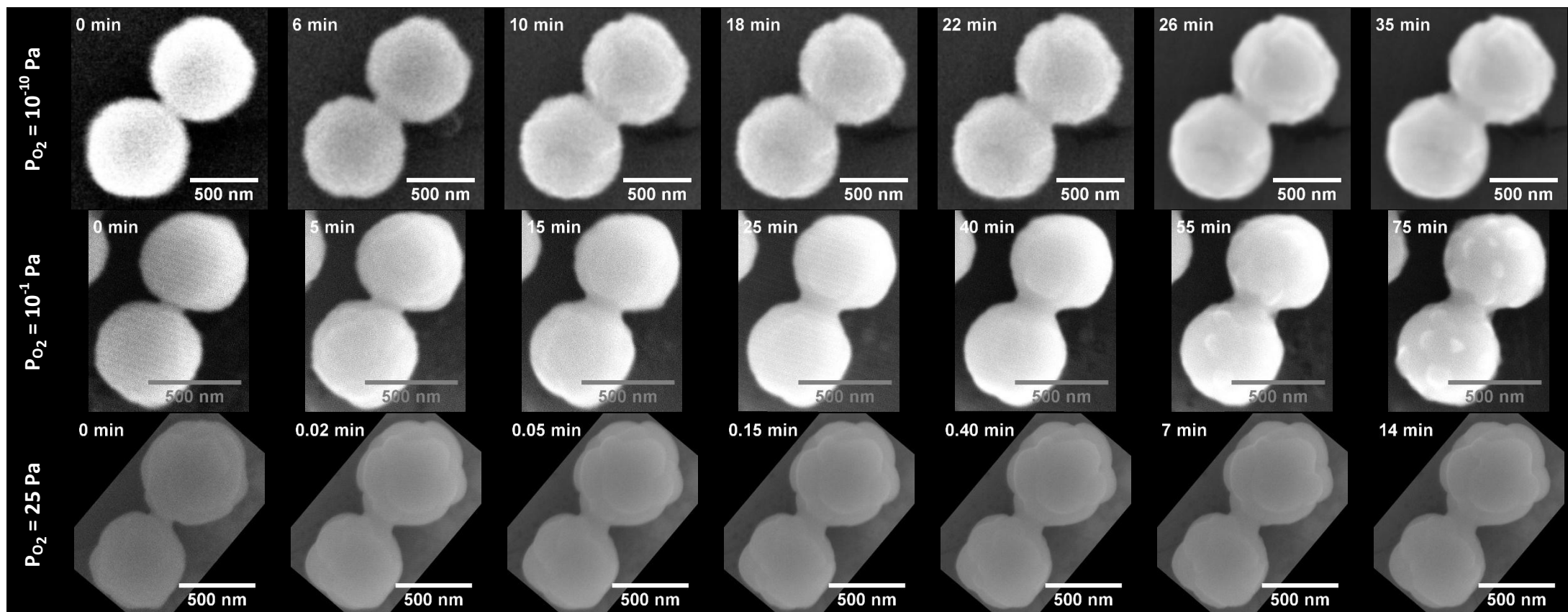


**Figure 4.** HT-ESEM images recorded *in situ* during heat treatment at 1000°C of uranium oxide microspheres under the various atmospheres studied.

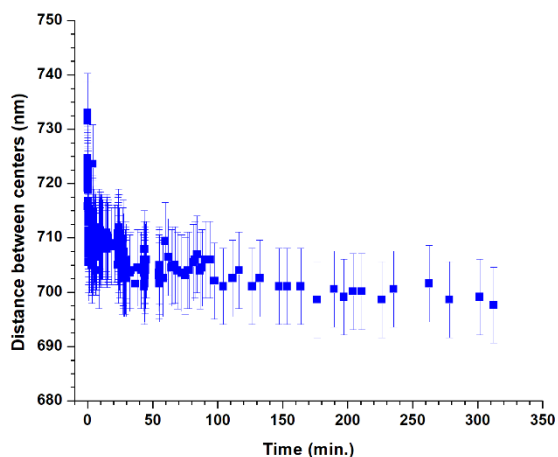
### 3.3. Kinetics of sintering first step

From the data reported in the previous section, neck formation and crystallites growth occurred systematically in the systems investigated, although with different kinetics. As such, the quantitative evaluation of geometrical parameters of interest was used to monitor the first step of sintering. Particularly, the diameter of the neck ( $x$ ) and the average diameter of the particles ( $r$ ) were measured, as well as the distance between the sphere centers ( $d$ ). Using this data, it was possible to calculate and plot the evolution of the dimensionless parameter  $\lambda$ , called sintering degree, and generally used to describe the first stage of sintering at the grain scale:

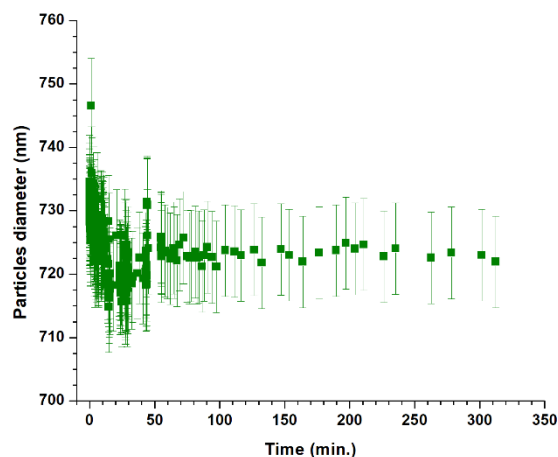
$$\lambda = x/r \quad (1.)$$

**Figure 5** reports the evolution of both  $x$ ,  $r$ ,  $d$  and  $\lambda$  parameters during the heat treatment of the particles at 830°C under air ( $P_{O_2} = 25$  Pa). In this example, which reflected most of the data collected, the diameter of the spherical particles used during the study remained mostly unchanged. Indeed, only a 3% diameter decrease was stated, which was ascribed to the volatilization of residual water and organics trapped in the microstructure, as well as to the elimination of inner porosity initially present in the particles. Simultaneously, the distance between the centers of the particles decreased by around 5%, thus attesting that densification of the system already started. Finally, the growth of the neck between the grains was observed during the first 60 minutes of the heat treatment, then reached a steady-state. As the variation of the grain size could be considered as negligible, the variation of the  $\lambda$  parameter followed the same trend, and reached a steady state after around 60 minutes of heating.

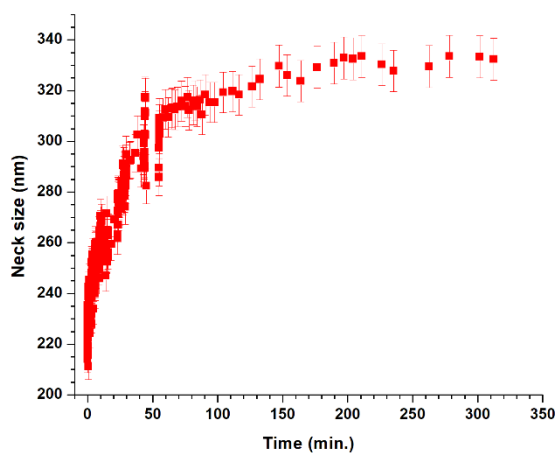
a)



b)



c)



d)

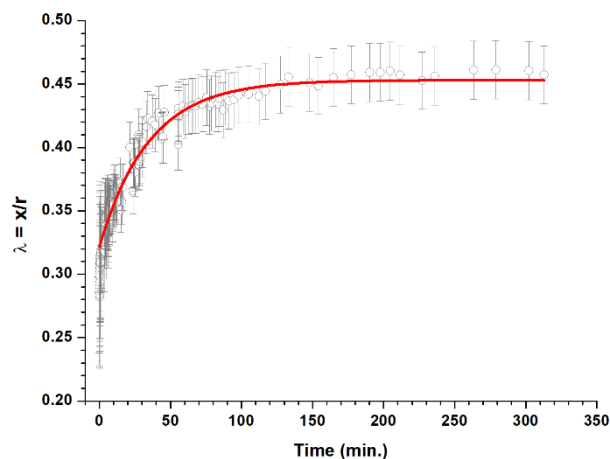


**Figure 5.** Evolution of the distance between the grains centers,  $d$ , (a) ; average grain diameter,  $r$  (b) ; neck diameter,  $x$ , (c) ; and dimensionless parameter,  $\lambda$ , (d) during heat treatment of the 700 nm-diameter particles at 830°C under air ( $P_{O_2} = 25$  Pa).

In order to directly visualize the effect of the atmosphere on the sintering kinetics, the evolution of the  $\lambda$  parameter at 1000°C was plotted in **Figure 6** for the three values of  $P_{O_2}$ . As already stated, the general behavior observed was similar in all the cases, with the variation controlled by the growth of the neck between the two spherical particles, the diameter of these latter being mostly unchanged. Nevertheless, the kinetics appeared to be strongly modified by the dioxygen partial pressure. In this example, an equilibrium state was reached in less than 10 minutes under air ( $P_{O_2} = 25$  Pa). Conversely, the process slowed down when  $P_{O_2}$  decreased (i.e.  $P_{O_2} = 10^{-1}$  Pa) while no steady-state was observed after 2 hours of heating treatment with  $P_{O_2} = 10^{-10}$  Pa.

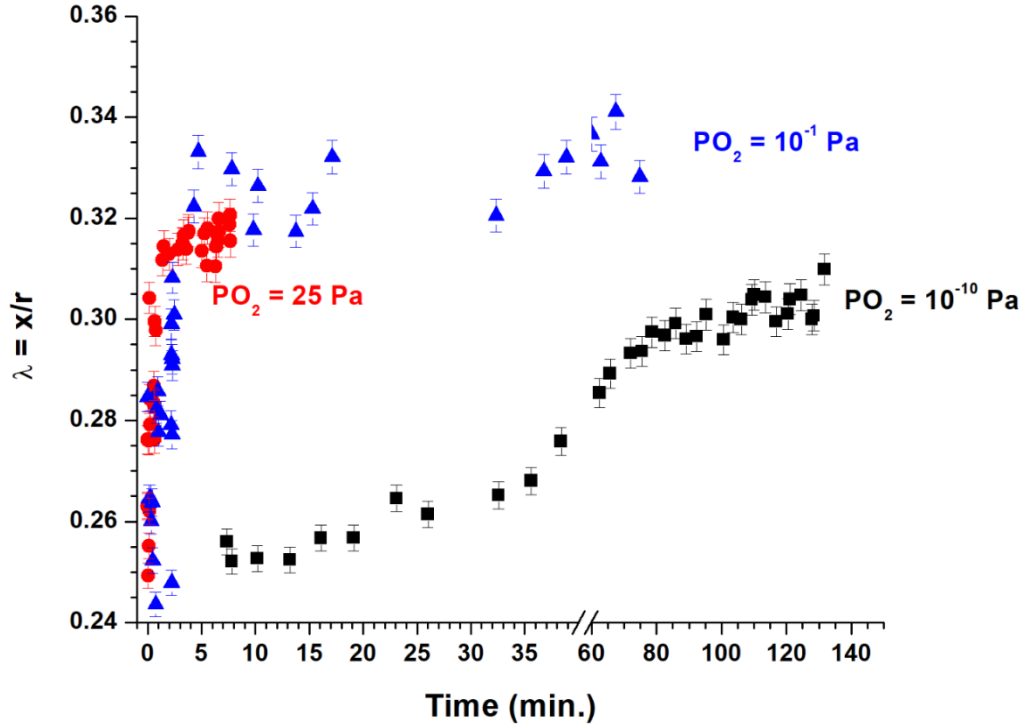


**Figure 6.** Evolution of the dimensionless parameter  $\lambda = x/r$  obtained at 1000°C for  $P_{O_2} = 10^{-10}$  Pa (■);  $10^{-1}$  Pa (▲) and 25 Pa (●).

The kinetic constants associated to the elaboration of the neck during the first step of the sintering were then determined by fitting the experimental data. From a mathematical point of view, our datasets can be fitted either with an exponential or a power law. Both kinds of models led to satisfactory correlation factors (i.e. typically around 0.9), which quality is mainly impacted by the scattering of the experimental data. From the physico-chemical point of view, the general model of neck growth developed during the 1950's [39], is based on a power law such as :

$$\lambda^n = \frac{k.t}{r^m} \quad (2.)$$

where  $\lambda = x/r$  is the dimensionless parameter describing the sintering degree,  $k$  is a kinetic constant,  $t$  is the duration of heat treatment, and  $n$  and  $m$  are exponents characteristic of the diffusion process involved (i.e. mainly surface, volume or grain boundary diffusion).

Nevertheless, this model was based on the hypothesis of single-crystal grains, which is not the case in this study, as the spherical particles used herein were clearly shown to be

polycrystalline. As the evolution of  $\lambda$  cannot be described by usual sintering models in the case of polycrystalline particles, we used a first-order kinetic law to fit the datasets obtained through HT-ESEM observations the evolution of the system, with:

$$\lambda = [a]_0 \times \exp^{-kt} + \lambda_0 \quad (3.)$$

where  $[a]_0$  is a pre-exponential factor,  $\lambda_0$  the sintering degree at  $t = 0$ , and  $k$  the kinetic constant (expressed in  $s^{-1}$ ).

This approach was already used successfully during the study of early stages of  $CeO_2$  and  $ThO_2$  [15, 16], and again led herein to good correlation factors (typically  $\geq 0.9$ ) for all the experimental conditions investigated, as evidenced on **Figure 5d**. It was then possible to assess the value of the kinetic constant associated to the elaboration of the neck between the two spherical particles for all the operating conditions considered in terms of temperature and  $P_{O_2}$  (**Table 3**).

**Table 3.** Summary of the kinetic constants determined for various operating conditions.

$P_{O_2} = 10^{-10} \text{ Pa}$		$P_{O_2} = 10^{-1} \text{ Pa}$		$P_{O_2} = 25 \text{ Pa}$	
T (°C)	k ( $s^{-1}$ )	T (°C)	k ( $s^{-1}$ )	T (°C)	k ( $s^{-1}$ )
885	$0.025 \pm 0.004$	925	$0.0080 \pm 0.0005$	830	$0.028 \pm 0.006$
900	$0.03 \pm 0.01$	950	$0.104 \pm 0.001$	870	$0.08 \pm 0.01$
920	$0.033 \pm 0.003$	965	$0.028 \pm 0.005$	910	$0.092 \pm 0.005$
950	$0.035 \pm 0.003$	980	$0.039 \pm 0.007$	930	$0.114 \pm 0.005$
965	$0.060 \pm 0.002$	1000	$0.11 \pm 0.03$	950	$0.35 \pm 0.02$
1010	$0.157 \pm 0.002$	1050	$0.19 \pm 0.02$	980	$0.70 \pm 0.04$
1050	$0.388 \pm 0.001$			1000	$1.5 \pm 0.1$

### 3.4. Determination of the activation energy

The kinetic constant determined for all the conditions in terms of temperature and atmosphere were further plotted in an Arrhenius diagram (**Figure 7**). For the three values of  $P_{O_2}$  investigated, the variation of  $\ln(k)$  versus the reciprocal temperature followed a linear trend, showing that the first step of sintering was driven by an unique diffusion mechanism on the interval of temperatures considered (typically 800-1100°C). This observation then contradicted the results reported by Lahiri *et al.* who pointed out a modification of the

diffusion mechanism operating during the sintering of stoichiometric  $\text{UO}_{2.00}$  around  $1050^\circ\text{C}$  [5].

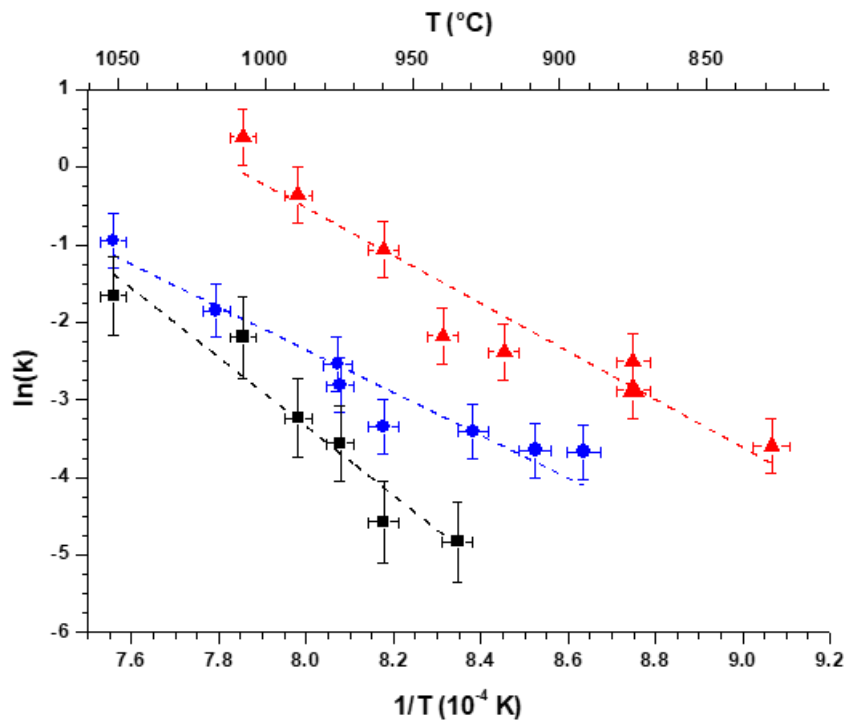


**Figure 7.** Variation of  $\ln(k)$  versus the reciprocal temperature associated to the first step of sintering of uranium oxides for various dioxygen partial pressures :  $P_{\text{O}_2} = 10^{-10}$  Pa (■);  $P_{\text{O}_2} = 10^{-1}$  Pa (●) and  $P_{\text{O}_2} = 25$  Pa (▲).

The activation energies calculated from the variation of the kinetic constant in the three atmospheres investigated are gathered in **Table 4**. Several authors already reported  $E_A$  values attached to the first step of the sintering of uranium dioxides. They systematically used bulky samples (i.e. pellets) and mostly based their works on dilatometry measurements through different methods such as Dorn's or Constant Heating Rate (CHR). The first studies undertaken in the 1960's led to extremely scattered results, with values ranging from 80 to  $460 \text{ kJ}\cdot\text{mol}^{-1}$  [40],[41]. Improving the control on the samples stoichiometry further led to more accurate measurements and allowed to reach a consensus on several points. First, the activation energy attached to the first step of sintering for a stoichiometric  $\text{UO}_{2.00}$  was generally reported around  $390\text{-}400 \text{ kJ}\cdot\text{mol}^{-1}$  [10], while it decreased when the oxide becomes hyper-stoichiometric, with values typically around  $220 \text{ kJ}\cdot\text{mol}^{-1}$  for  $2.002 < \text{O/U} < 2.1$  [2, 42]. Nevertheless, some uncertainties still persisted in the accurate determination of the O/U ratio in these samples. Also, the temperature ranges studied were wide, which could have led to

encompass both neck elaboration and densification/grain growth phenomena. As such, Ainscough *et al.* showed that an activation energy of  $260 \text{ kJ}\cdot\text{mol}^{-1}$ , very close to those cited above, was obtained when studying grain growth in a  $\text{UO}_{2.00}$  pellet between  $1300$  and  $1500^\circ\text{C}$  [43]. Actually, the activation energy only differed significantly when reaching very high temperatures, where the processes observed became easily discernable from the first step of sintering. As a matter of example, Singh concluded to a value close to  $500 \text{ kJ}\cdot\text{mol}^{-1}$  between  $1800$  and  $2100^\circ\text{C}$  [44].

In order to overcome all these discrepancies, more recent works reinvestigated critically the first step of  $\text{UO}_{2+x}$  sintering, with the aim to specify the driving mechanism and associated activation energies. The values gathered in the review by Knorr *et al.* [14], as well as those determined by Dehaut *et al.* through different methods [3], then seemed to be the most accurate available up to date, and will be used as references. Also, these authors explored the upper range of the  $\text{UO}_{2+x}$  stoichiometry (i.e. typically  $x > 0.15$ ), which was previously poorly documented.

**Table 4.** Activation energies associated to the first step of sintering for various uranium oxides stabilized in our operating conditions.

$\text{P}_{\text{O}_2}$ (Pa)	Atmosphere	Oxide	Activation energy ( $\text{kJ}\cdot\text{mol}^{-1}$ )
25	120 Pa Air	$\text{U}_3\text{O}_8$	$260 \pm 40$
$10^{-1}$	100 Pa $\text{N}_2$ / 1000 ppm $\text{O}_2$	$\text{UO}_{2.21}$	$370 \pm 50$
$10^{-10}$	150 Pa $\text{N}_2$ / 5% $\text{H}_2$ / 0,2% ppm $\text{H}_2\text{O}$	$\text{UO}_{2.01}$	$210 \pm 25$

The activation energies calculated in this study were generally found to be in very good agreement with the reference data selected in the literature. A very small hyper-stoichiometry ( $x = 0.01$ ) was associated to the lowest value of  $E_A$ , close to  $200 \text{ kJ}\cdot\text{mol}^{-1}$ . Conversely, regarding to highly hyper-stoichiometric  $\text{UO}_{2+x}$ , the value determined for  $\text{UO}_{2.21}$  was found between those published for  $\text{UO}_{2.17}$  and  $\text{UO}_{2.22}$  by Dehaut *et al.* ( $323$  and  $437 \text{ kJ}\cdot\text{mol}^{-1}$ , respectively) [3]. Nevertheless, it did not comply with the hypothesis of a threshold between these compositions linked with the structural transition from  $\text{UO}_{2+x}$  to  $\text{U}_4\text{O}_9$ , and to the subsequent modification of uranium diffusion coefficient. Finally, to the best of our knowledge, the value determined for the first step of  $\text{U}_3\text{O}_8$  sintering ( $260 \text{ kJ}\cdot\text{mol}^{-1}$ ) is the first to be published. It is close to that generally reported for uranium dioxides exhibiting O/U ratios close to 2, and then appears to be significantly lower than those of

UO<sub>2.00</sub> and U<sub>4</sub>O<sub>9</sub>. This result then backs up the use of U<sub>3</sub>O<sub>8</sub> as a sintering aid during the fabrication process of UOx or MOx fuels, particularly when recycling scraps [45, 46].

Also, it is important to underline that the values obtained in this study could be considered as references for further works. First, the characterization technique used for the determination of the data allowed us to unambiguously discriminate the first step of sintering, as only geometrical measurements coming from neck elaboration were considered. Also, the stoichiometry of the samples was fixed through the monitoring of the surrounding atmosphere in the HT-ESEM chamber, then checked by both theoretical and experimental means. Moreover, the sub-micrometric size of our sample led us to prevent any stoichiometry gradient effect in the solid phase, which could not have been excluded when working with bulk samples, especially when preparing the materials through powder metallurgy processes.

### 3.5. Diffusion mechanism

Sintering of ceramics can be driven by different diffusion processes, i.e. surface diffusion, volume diffusion, grain boundary diffusion, evaporation-condensation and viscous flow. Only three of these mass transport mechanisms take part in the densification of the sample: grain boundary diffusion, volume diffusion and, in the case of liquid phase sintering, viscous flow. In our study, this densification was evidenced by the decrease of the distance between the centers of the two spherical particles of uranium oxides (**Figure 5a**).

The prevailing diffusion mechanism driving the sintering of a ceramic material is generally evidenced by determining the values of the  $m$  and  $n$  exponents involved in the general kinetic law used to describe the neck elaboration (eq. 2). However, as stated before, this equation cannot be applied to our polycrystalline particles. For such systems, we therefore used the Herring's scaling law, which expresses the influence of particles size on the microstructural modifications of the sample during sintering. For grains presenting similar shapes, although with different sizes, sintered in identical experimental conditions, the Herring's scaling law predicts the relative time required to reach a given sintering degree (i.e. same  $\lambda$  value) [47]. When considering two spherical grains in contact with different radii, the following expression can be established [48] :

$$\frac{t_1}{t_2} = \left(\frac{r_1}{r_2}\right)^m \quad (4.)$$

Where  $r_1$  and  $r_2$  are the grains radii,  $t_1$  and  $t_2$  the sintering times, and  $m$  an exponent specific to the diffusion mechanism operating during sintering, with  $m = 1$  for viscous flow;  $m = 2$  for evaporation-condensation;  $m = 3$  for volume diffusion and  $m = 4$  for surface diffusion or grain boundary diffusion.

Different experiments were then undertaken, starting with uranium oxide microspheres presenting diameters of 700 and 1400 nm. The comparison of the results obtained for the two systems during a heating treatment at 930°C under air ( $P_{O_2} = 25$  Pa) is provided in **Figure 8** as an example. As expected from the general kinetic laws of sintering, which are systematically proportional to  $(1/r)$ , the two-grains system composed of the smallest particles evolved more rapidly. Two values of  $\lambda$  reached by the two systems were then selected arbitrarily and the associated times were determined. These data, gathered in **Table 5**, allowed us to determine  $m$  values close to 3, which accounted for volume diffusion.

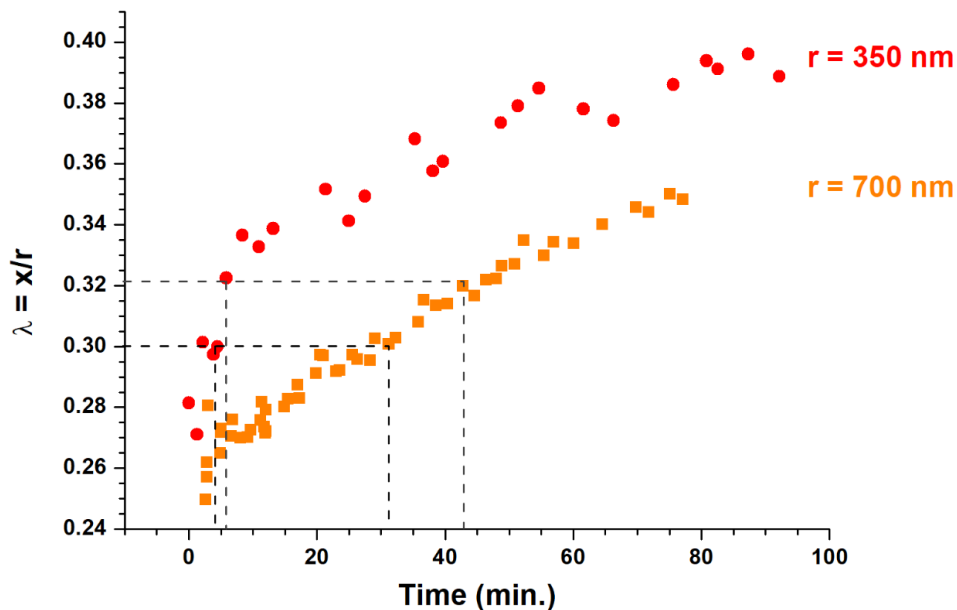


**Figure 8.** Compared evolution of the  $\lambda$  parameter at  $T = 930^\circ\text{C}$  and  $P_{O_2} = 25$  Pa for systems composed of spherical particles of 700 nm (●) and 1400 nm (■) in diameter.

More importantly, similar results were obtained whatever the atmosphere considered, and thus whatever the dioxygen partial pressure. Hence, in the range of temperatures considered, the mechanism driving the first step of sintering was not significantly modified by the experimental conditions. It remained controlled by volume diffusion. This result contradicted previous reports attesting of the prevalence of grain boundary diffusion during

the sintering of  $\text{UO}_{2+x}$  [2]. Nevertheless, it is worth noting that all these studies were based on the use of bulk samples, which could have led to convolute different phenomena occurring during the heating treatment of the ceramic material, particularly neck formation and grain growth. Nevertheless, such a discrepancy was not mentioned in our previous works, where HT-ESEM studies of  $\text{CeO}_2$  and  $\text{ThO}_2$  both concluded to grain boundary diffusion as the driving mechanism of the first step of sintering [15, 16].

On this basis, it is important to remember that several diffusion mechanisms always operate simultaneously during the sintering of ceramic or metallic materials. In the case of uranium oxides, it is then likely that volume and grain boundary diffusion present comparable contributions to the global kinetics. The modification of experimental parameters, such as the temperature, the atmosphere, or the grain size, could then generate inversion in the prevailing diffusion path. As such, the use of sub-micrometric particles in our study could be considered as one important explanation to the differences observed with other works employing bulk materials composed of micrometric grains. In these conditions, it is crucial to consider all the diffusive processes possible when modeling the first step of sintering. This is particularly the case for  $\text{UO}_{2+x}$ , for which the models frequently consider surface and grain boundary diffusion but neglect volume diffusion [49].

**Table 5.** Summary of the values obtained for the determination of the prevailing mechanism operating during the first step of uranium oxide sintering in the different atmospheres investigated.

$x/r$	$t_1$ - 700 nm (min.)	$t_2$ - 1400 nm (min.)	$m$
<b>1010°C – <math>P_{\text{O}_2} = 10^{-10}</math> Pa</b>			
0.208	3.05	21.75	2.83
0.203	2.65	26.42	3.32
<b>1050°C – <math>P_{\text{O}_2} = 10^{-1}</math> Pa</b>			
0.3	5.93	50.48	3.09
0.285	4.48	36.53	3.03
<b>930 °C – <math>P_{\text{O}_2} = 25</math> Pa</b>			
0.32	5.85	48.05	3.04
0.3	3.83	25.57	2.74

## Conclusion

The first step of the sintering of various uranium oxides was monitored *in situ* for the first time through HT-ESEM observations, allowing to evidence directly the impact of the dioxygen partial pressure over the kinetics of neck elaboration. In all the operating conditions tested, image processing led to the determination of quantitative data describing the evolution of two-grain systems morphology. Although the growth of the nanometric crystallites composing the spherical grains was not followed in this study, the formation and the development of a neck between the particles was clearly evidenced. It was not accompanied by a significant decrease of the grains diameter, even if deformation was noted under the most oxidative atmosphere studied.

As the polycrystalline systems studied herein doesn't comply with the general kinetic laws of sintering, the evolution of the  $\lambda$  dimensionless parameter describing the sintering advancement was fitted using a simple first-order law. It first allowed us to evaluate the activation energy attached to the first step of sintering in the different conditions tested. When the dioxygen partial pressure led to stabilize hyper-stoichiometric  $\text{UO}_{2+x}$  oxides, the values obtained were found to increase with  $x$ , typically in the 200-400  $\text{kJ}\cdot\text{mol}^{-1}$  range. Also, since the experimental technique used in this study strictly addressed the first step of sintering, i.e. formation of a neck between the particles, these values led to clear up the scattered data present in the literature and comforted some of the most recent studies. Under air atmosphere, the stabilization of  $\text{U}_3\text{O}_8$  allowed us to provide the first evaluation of activation energy for the first step of sintering. This latter was close to that obtained for  $\text{UO}_{2+x}$  for low values of  $x$ , and was thus significantly lower than that obtained for stoichiometric  $\text{UO}_{2.00}$  and  $\text{U}_4\text{O}_9$ . This result then supports the use of  $\text{U}_3\text{O}_8$  as an aid for the sintering of oxide nuclear fuel pellets, especially when recycling scraps. According to the Herring scaling law, the main diffusion mechanism driving the first step of sintering was volume diffusion, independently from the stoichiometry of the uranium oxide. This work then provides an original set of data that can be implemented in numerical models describing the sintering of  $\text{UO}_{2+x}$ .

## Acknowledgments

Authors would like to thank M. Ibrahim Osman (ICSM/LIME) for his help during HT-ESEM observations as well as X.F. Le Goff and H.P. Brau (ICSM/L2ME) for their support in the processing of the SEM images. PhD of V. Trillaud was funded by CEA. This work also received funding from the GENIORS project (H2020 Euratom Research and Innovation Programme under grant agreement n°755171).

## References

- [1] J.E. Kelly, Generation IV International Forum: A decade of progress through international cooperation, *Prog Nucl Energ*, 77 (2014) 240-246.
- [2] M.J. Bannister, W.J. Buykx, Sintering Mechanism in  $\text{UO}_{2+x}$ , *J Nucl Mater*, 64 (1977) 57-65.
- [3] P. Dehaut, L. Bourgeois, H. Chevrel, Activation energy of  $\text{UO}_2$  and  $\text{UO}_{2+x}$  sintering, *J Nucl Mater*, 299 (2001) 250-259.
- [4] A. Mohan, N.C. Soni, V.K. Moorthy, Sintering Diagrams of  $\text{UO}_2$ , *J Nucl Mater*, 79 (1979) 312-322.
- [5] D. Lahiri, S.V.R. Rao, G.V.S.H. Rao, R.K. Srivastava, Study on sintering kinetics and activation energy of  $\text{UO}_2$  pellets using three different methods, *J Nucl Mater*, 357 (2006) 88-96.
- [6] F. Wakai, Modeling and simulation of elementary processes in ideal sintering, *J Am Ceram Soc*, 89 (2006) 1471-1484.
- [7] S. Bordere, D. Bernard, Full resolution of the Monte Carlo time scale demonstrated through the modelling of two-amorphous-particles sintering, *Comp Mater Sci*, 43 (2008) 1074-1080.
- [8] S. Martin, R. Parekh, M. Guessasma, J. Lechelle, J. Fortin, K. Saleh, Study of the sintering kinetics of bimodal powders. A parametric DEM study, *Powder Technol*, 270 (2015) 637-645.
- [9] M. El-Sayed Ali, R. Lorenzelli, Kinetics of Initial-Stage of Sintering of  $\text{UO}_2$  and  $\text{UO}_2$  with  $\text{Nd}_2\text{O}_3$  Addition, *J Nucl Mater*, 87 (1979) 90-96.
- [10] J.J. Bacmann, G. Cizeron, Mechanisms in Incipient Uranium Dioxide Calcination, *J Nucl Mater*, 33 (1969) 271-285.
- [11] J.L. Woolfrey, Effect of Green Density on Initial-Stage Sintering Kinetics of  $\text{UO}_2$ , *J Am Ceram Soc*, 55 (1972) 383-389.
- [12] B. Burton, G.L. Reynolds, Influence of Deviations from Stoichiometric Composition on Diffusional Creep of Uranium-Dioxide, *Acta Metallurgica*, 21 (1973) 1641-1647.
- [13] T.R.G. Kutty, P.V. Hegde, K.B. Khan, U. Basak, S.N. Pillai, A.K. Sengupta, G.C. Jain, S. Majumdar, H.S. Kamath, D.S.C. Purushotham, Densification behaviour of  $\text{UO}_2$  in six different atmospheres, *J Nucl Mater*, 305 (2002) 159-168.
- [14] D.B. Knorr, R.M. Cannon, R.L. Coble, An Analysis of Diffusion and Diffusional Creep in Stoichiometric and Hyperstoichiometric Uranium-Dioxide, *Acta Metallurgica*, 37 (1989) 2103-2123.
- [15] G.I. Nkou Bouala, N. Clavier, S. Martin, J. Lechelle, J. Favrichon, H.P. Brau, N. Dacheux, R. Podor, From in Situ HT-ESEM Observations to Simulation: How Does

- Polycrystallinity Affects the Sintering of CeO<sub>2</sub> Microspheres?, *J Phys Chem C*, 120 (2016) 386-395.
- [16] G.I. Nkou Bouala, N. Clavier, J. Lechelle, J. Monnier, C. Ricolleau, N. Dacheux, R. Podor, High-temperature electron microscopy study of ThO<sub>2</sub> microspheres sintering, *J Eur Ceram Soc*, 37 (2017) 727-738.
- [17] V. Trillaud, J. Maynadie, J. Manaud, J. Hidalgo, D. Meyer, R. Podor, N. Dacheux, N. Clavier, Synthesis of size-controlled UO<sub>2</sub> microspheres from the hydrothermal conversion of U(IV) aspartate, *Crystengcomm*, 20 (2018) 7749-7760.
- [18] N. Dacheux, V. Brandel, M. Genet, Synthesis and Properties of Uranium Chloride Phosphate Tetrahydrate - UCiPO<sub>4</sub>.4H<sub>2</sub>O, *New J Chem*, 19 (1995) 1029-1036.
- [19] P. Thompson, D.E. Cox, J.B. Hastings, Rietveld Refinement of Debye-Scherrer Synchrotron X-Ray Data from Al<sub>2</sub>O<sub>3</sub>, *J Appl Crystallogr*, 20 (1987) 79-83.
- [20] C. Frontera, J. Rodriguez-Carvajal, FullProf as a new tool for flipping ratio analysis, *Physica B: Condensed Matter*, 335 (2003) 219-222.
- [21] R. Podor, G.I. Nkou Bouala, J. Ravaux, J. Lautru, N. Clavier, Working with the ESEM at high temperature, *Mater Charact*, 151 (2019) 15-26.
- [22] R. Podor, D. Pailhon, J. Ravaux, H.P. Brau, Development of an Integrated Thermocouple for the Accurate Sample Temperature Measurement During High Temperature Environmental Scanning Electron Microscopy (HT-ESEM) Experiments, *Microscopy and Microanalysis*, 21 (2015) 307-312.
- [23] FURNASEM, <https://newtec.fr/en/furnasem2/> (accessed 07.10.2020)
- [24] L. Joly-Pottuz, A. Bogner, A. Lasalle, A. Malchere, G. Thollet, S. Deville, Improvements for imaging ceramics sintering in situ in ESEM, *J Microsc-Oxford*, 244 (2011) 93-100.
- [25] J. Pascau, J.M. Mateos Perez, Image processing with ImageJ, Birmingham, UK, 2013.
- [26] C.A. Schneider, W.S. Rasband, K.W. Eliceiri, NIH Image to ImageJ: 25 years of image analysis, *Nature Methods*, 9 (2012) 671-675.
- [27] J. Favrichon, Imageju, <https://github.com/jfavrichon/imageju> (accessed 07.10.2020)
- [28] N. Saunders, A.P. Miodownik, CALPHAD (Calculation of Phase Diagrams): A Comprehensive Guide, Pergamon, 1998.
- [29] C. Gueneau, N. Dupin, B. Sundman, C. Martial, J.C. Dumas, S. Gosse, S. Chatain, F. De Bruycker, D. Manara, R.J.M. Konings, Thermodynamic modelling of advanced oxide and carbide nuclear fuels: Description of the U-Pu-O-C systems, *J Nucl Mater*, 419 (2011) 145-167.
- [30] L. Desgranges, G. Badinozzi, D. Simeone, H.E. Fischer, Refinement of the  $\alpha$ -U<sub>4</sub>O<sub>9</sub> Crystalline Structure: New Insight into the U<sub>4</sub>O<sub>9</sub> -> U<sub>3</sub>O<sub>8</sub> Transformation, *Inorg Chem*, 50 (2011) 6146-6151.
- [31] J.M. Elorrieta, L.J. Bonales, N. Rodriguez-Villagra, V.G. Baonza, J. Cobos, A detailed Raman and X-Ray study of UO<sub>2+x</sub> oxides and related structure transitions, *Phys Chem Chem Phys*, 18 (2016) 28209-28216.
- [32] K.O. Kvashnina, S.M. Butorin, P. Martin, P. Glatzel, Chemical State of Complex Uranium Oxides, *Phys Rev Lett*, 111 (2013) 253002.
- [33] G. Leinders, T. Cardinaels, K. Binnemans, M. Verwerft, Accurate lattice parameter measurements of stoichiometric uranium dioxide, *J Nucl Mater*, 459 (2015) 135-142.
- [34] R.J. McEachern, P. Taylor, A review of the oxidation of uranium dioxide at temperatures below 400°C, *J Nucl Mater*, 254 (1998) 87-121.

- [35] F. Grønvold, High-Temperature X-Ray Study of Uranium Oxides in the  $\text{UO}_2\text{-U}_3\text{O}_8$  Region, *J Inorg Nucl Chem*, 1 (1955) 357-370.
- [36] B.O. Loopstra, Phase Transition in  $\alpha\text{-U}_3\text{O}_8$  at 210°C, *J Appl Crystallogr*, 3 (1970) 94-96.
- [37] S.A. Utlak, J.W. McMurray, Thermodynamic modeling of the  $\text{U}_3\text{O}_{8-x}$  solid solution phase, *J Nucl Mater*, 530 (2020).
- [38] L. Quemard, L. Desgranges, V. Bouineau, M. Pijolat, G. Baldinozzi, N. Millot, J.C. Niepce, A. Poulesquen, On the origin of the sigmoid shape in the  $\text{UO}_2$  oxidation weight gain curves, *J Eur Ceram Soc*, 29 (2009) 2791-2798.
- [39] G.C. Kuczynski, The Mechanism of Densification during Sintering of Metallic Particles, *Acta Metallurgica*, 4 (1956) 58-61.
- [40] M.M. Ristic, E. Kostic, Etude du procédé de frittage du dioxyde d'uranium d'après la théorie de Pines, *Nuclear Science Abstracts*, 18 (1964) NP-14124.
- [41] K.W. Lay, R.E. Carter, Role of O/U Ratio on Sintering of  $\text{UO}_2$ , *J Nucl Mater*, 30 (1969) 74-87.
- [42] L. Halldahl, Quasi-Isothermal Dilatometric Sintering Studies on  $\text{UO}_2$  Powder Compacts - Method of Evaluation and Influence of Experimental Parameters, *Thermochim Acta*, 58 (1982) 261-270.
- [43] J.B. Ainscough, B.W. Oldfield, J.O. Ware, Isothermal Grain-Growth Kinetics in Sintered  $\text{UO}_2$  Pellets, *J Nucl Mater*, 49 (1973) 117-128.
- [44] R.N. Singh, Isothermal Grain-Growth Kinetics in Sintered  $\text{UO}_2$  Pellets, *J Nucl Mater*, 64 (1977) 174-178.
- [45] J.H. Yang, K.W. Kang, K.S. Kim, Y.W. Rhee, K.W. Song, Recycling Process for Sinter-Active  $\text{U}_3\text{O}_8$  Powders, *J Nucl Sci Technol*, 47 (2010) 538-541.
- [46] K.W. Song, K.S. Kim, Y.M. Kim, Y.H. Jung, Sintering of mixed  $\text{UO}_2$  and  $\text{U}_3\text{O}_8$  powder compacts, *J Nucl Mater*, 277 (2000) 123-129.
- [47] C. Herring, Effect of Change of Scale on Sintering Phenomena, *J Appl Phys*, 21 (1950) 301-303.
- [48] M. Lequitte, D. Autissier, Synthesis and sintering of nanocrystalline erbium oxide, *Nanostruct Mater*, 6 (1995) 333-336.
- [49] J. Lechelle, R. Boyer, M. Trotabas, A mechanistic approach of the sintering of nuclear fuel ceramics, *Mater Chem Phys*, 67 (2001) 120-132.

## Supporting information

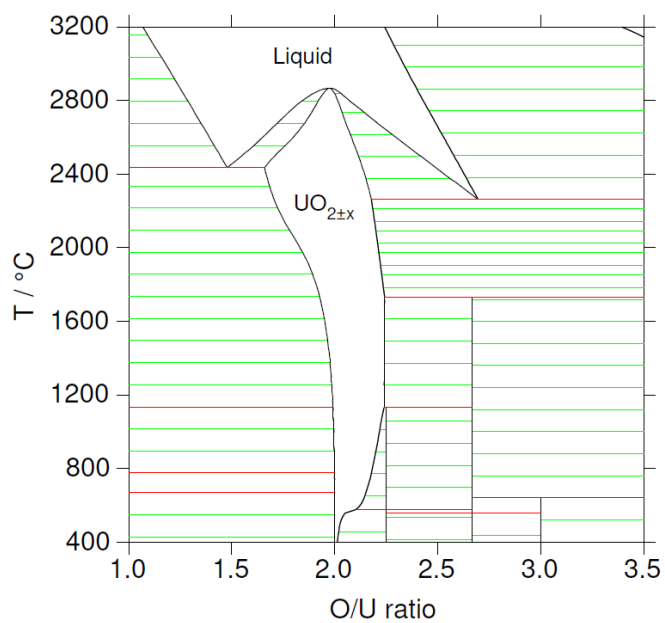


**Figure S1.** Portions of the U-O phase diagram calculated after Guéneau et al. [29] The maximum hyper-stoichiometry of the fluorite-type structure of UO<sub>2±x</sub> is around 2.24 above the decomposition temperature of U<sub>4</sub>O<sub>9</sub> (T = 1131°C).